Faint and clustered components in exponential analysis

Annie Cuyt[a], Min-nan Tsai[a,b], Marleen Verhoye[c], Wen-shin Lee[a,*]

[a] Department of Mathematics and Computer Science, University of Antwerp, Belgium
[b] Department of Computer Science and Information Engineering, National Taiwan Normal University, Taiwan
[c] Bio-Imaging Lab, University of Antwerp, Belgium

A R T I C L E   I N F O

A B S T R A C T

An important hurdle in multi-exponential analysis is the correct detection of the number of components in a multi-exponential signal and their subsequent identification. This is especially difficult if one or more of these terms are faint and/or covered by noise. We present an approach to tackle this problem and illustrate its usefulness in motor current signature analysis (MCSA), relaxometry (in FLIM and MRI) and magnetic resonance spectroscopy (MRS).

The approach is based on viewing the exponential analysis as a Padé approximation problem and makes use of some well-known theorems from Padé approximation theory. We show how to achieve a clear separation of signal and noise by computing sufficiently high order Padé approximants, thus modeling both the signal and the noise, rather than filtering out the noise at an earlier stage and return a low order approximant.

We illustrate the usefulness of the approach in different practical situations, where some exponential components are difficult to detect and retrieve because they are either faint compared to the other signal elements or contained in a cluster of similar exponential components.

© 2017 Elsevier Inc. All rights reserved.

1. Introduction

Many real-time experiments involve the measurement of signals which fall exponentially with time. The problem is then to determine, from such measurements, the number of components n and the value of all the parameters in the exponential model

$$\phi(t) = \sum_{i=1}^{n} \alpha_i \exp(\phi_i t),$$
$$\alpha_i = \beta_i \exp(i\gamma_i), \quad \phi_i = \psi_i + i\omega_i, \quad i^2 = -1. \tag{1}$$

Here ψ_i, ω_i, β_i and γ_i are respectively called the damping, frequency, amplitude and phase of each exponential term. The technique of multi-exponential analysis is closely related to what is commonly known in the applied sciences as the Padé–Laplace method [2] and the technique of sparse interpolation in the field of symbolic computation [14].

The basic method to estimate the parameters in a sum of complex exponentials is due to Prony [29]. It was later refined by Pisarenko [27]. Modern computer implementations include the MUltiple SIgnal Classification algorithm MUSIC [31], the

---

* Corresponding author.
E-mail addresses: annie.cuyt@uantwerpen.be (A. Cuyt), edwen0224@gmail.com (M.-n. Tsai), marleen.verhoye@uantwerpen.be (M. Verhoye), wen-shin.lee@uantwerpen.be (W.-s. Lee).

Estimation of Signal Parameters via Rotational Invariance Techniques ESPRIT [30], the Toeplitz Approximation Method TAM [23] and the Matrix Pencil method MP [19].

The major hurdles in multi-exponential modelling are the correct detection of the number of components in the model, the noise sensitivity of problem statement and computational method, the limitation to distinguish closely spaced frequencies ω_i [8], and the difficulty in resolving different exponential decays ψ_i if the damping factors are too much alike [4].

Before we proceed, some words on Fourier methods are appropriate. Fourier analysis is not very well suited for the decomposition of aperiodic signals, such as exponentially decaying ones. The damping causes a broadening of the spectral peaks, which in its turn leads to the peaks overlapping and masking the smaller amplitude peaks. The latter are important for the fine level signal classification. Moreover, Fourier analysis completely ignores any actual physical multi-exponential structure of the encoded time signal.

Here we show how to make use of the connections between signal processing, Padé approximation and sparse interpolation to:

- retrieve the correct number of components in a signal.
- and the characteristics of faint components buried in noise.

How to regularize the exponential analysis problem statement and improve the ω_i- and ψ_i-resolution is dealt with in [10–12].

2. Exponential analysis and sparse interpolation

Let us assume that in $\phi(t)$ given by (1), the frequency content is limited by the bandwidth Ω,

$$|\Im(\phi_i)| = |\omega_i| < \Omega/2, \qquad i = 1, \ldots, n,$$

where $\Im(\cdot)$ denotes the imaginary part of a complex number. Also, let $\phi(t)$ be sampled at the equidistant points $t_j = j\Delta$ for $j = 0, 1, \ldots, 2n-1, \ldots$, with $\Delta < 2\pi/\Omega$ [25,32] in order to avoid aliasing effects in the analysis and reconstruction of $\phi(t)$. In the sequel we denote

$$f_j := \phi(t_j), \qquad j = 0, 1, \ldots, 2n-1, \ldots$$

We now summarize the exponential analysis method that underlies all modern implementations to extract $n, \phi_1, \ldots, \phi_n, \alpha_1, \ldots, \alpha_n$ from the uniformly taken measurements $f_0, \ldots, f_{2n-1}, \ldots$ and the specific form (1) of the model for $\phi(t)$.

2.1. Foundations of Prony's method

If we further denote

$$\lambda_i := \exp(\phi_i \Delta) = (\exp(\Delta))^{\phi_i},$$

then it is apparent that the data f_j are structured, namely

$$f_j = \sum_{i=1}^{n} \alpha_i \lambda_i^j, \qquad j = 0, \ldots, 2n-1, \ldots \qquad (2)$$

The system of equations (2) is called a sparse interpolation problem: the data f_j taken at the equidistant points $t_j = j\Delta$ are interpolated by the expression

$$\sum_{i=1}^{n} \alpha_i (\exp(t))^{\phi_i},$$

where the $\alpha_i, \phi_i, i = 1, \ldots, n$ are unknown.

Let us define the Hankel matrices

$$H_n^{(r)} := \begin{pmatrix} f_r & \cdots & f_{r+n-1} \\ \vdots & \ddots & \vdots \\ f_{r+n-1} & \cdots & f_{r+2n-2} \end{pmatrix}, \qquad r \geq 0.$$

It is known from [18, p. 603] that for the multi-exponential samples f_j given by (2),

$$\det H_\nu^{(r)} = 0, \quad \nu > n, \quad r \geq 0 \qquad (3)$$

$$\det H_n^{(r)} \neq 0, \quad r \geq 0 \qquad (4)$$

and it is proved in [21] that

$$\det H_\nu^{(r)} = 0 \text{ only accidentally}, \quad \nu < n. \qquad (5)$$
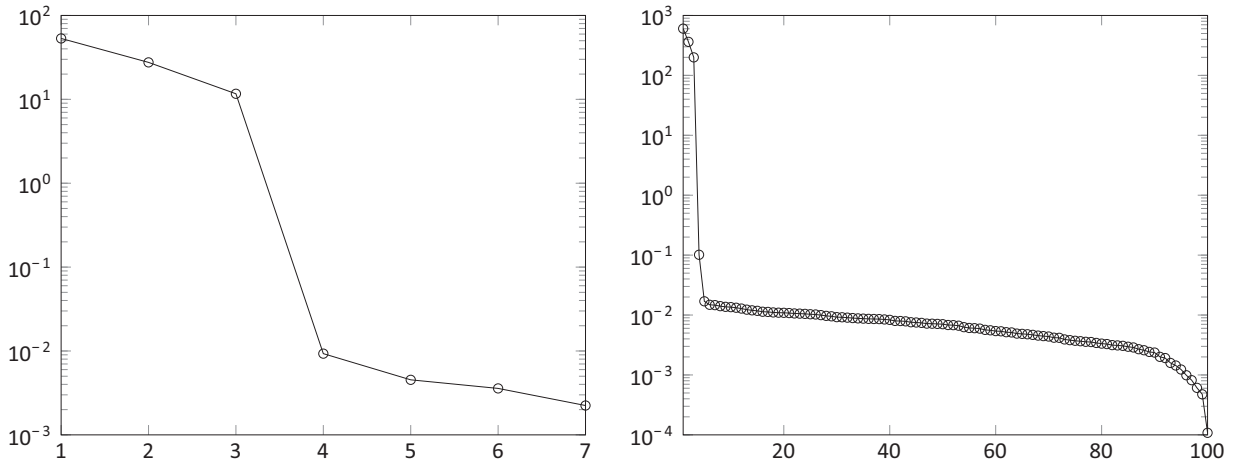
Fig. 1. Log-plot of singular values of $H_7^{(0)}$ and $H_{100}^{(0)}$ for $\phi(t)$ with added noise as described.

From these statements the number of components n can be obtained as the rank of $H_\nu^{(r)}$ for $\nu > n$. However, this method proves to be numerically unreliable in the presence of noise, as we illustrate with the computed example further down.

The λ_i can be retrieved [19] as the generalized eigenvalues of the problem

$$H_n^{(1)} v_i = \lambda_i H_n^{(0)} v_i, \quad i = 1, \dots, n, \tag{6}$$

where v_i are the generalized right eigenvectors. Then from the values λ_i, the ϕ_i can uniquely be retrieved because of the restriction $|\Im(\phi_i \Delta)| = |\omega_i| \Delta < (\Omega/2)(2\pi/\Omega) = \pi$.

To conclude, one finds the α_i from the interpolation conditions

$$\sum_{i=1}^{n} \alpha_i \exp(\phi_i t_j) = f_j, \quad j = 0, \dots, 2n - 1, \tag{7}$$

either by solving the system in the least squares sense (in the presence of noise) or by solving a subset of n consecutive interpolation conditions in case of a (mostly synthesized) noisefree $\phi(t)$. Note that

$$\exp(\phi_i t_j) = \exp(\phi_i j \Delta) = \lambda_i^j,$$

and that the coefficient matrix of (7) is therefore a Vandermonde matrix.

2.2. Challenge when components are faint or clustered

To give the reader some feeling about the numerical behaviour of (4)–(5), we consider the following example:

$$
\begin{aligned}
\phi_1 &= i3\pi, & \alpha_1 &= 10^{-3}, \\
\phi_2 &= i31.4\pi, & \alpha_2 &= 2, \\
\phi_3 &= -0.1 + i80\pi, & \alpha_3 &= 4, \\
\phi_4 &= -0.3 + i50.4\pi & \alpha_4 &= 8.
\end{aligned}
$$

We take the sampling interval $\Delta = 0.01$, which is in accordance with the Shannon–Nyquist requirement since $0.01 < 2\pi/\Omega = 0.0125\pi$.

In addition we add some realistic white circular Gaussian noise to each signal sample (mean 0, variance 1) and normalize the noise to have infinity-norm equal to 2×10^{-3}. The example is a challenge because most of the component $\alpha_1 \exp(\phi_1 t)$ is now buried in the noise. In Fig. 1 (left) we display the singular values of $H_\nu^{(0)}$ for $\nu = 7 > n = 4$. The log-scale plot indicates a numerical rank of 3 instead of the correct 4. This coincides with the result found when using the Padé algorithms in [17] and [20]: choosing the threshold parameter in [17] larger than or equal to 5×10^{-5} results in a numerical rank for $H_7^{(0)}$ of 3, while choosing it less than or equal to 1×10^{-5} returns a numerical rank of 7 while the correct value is 4.
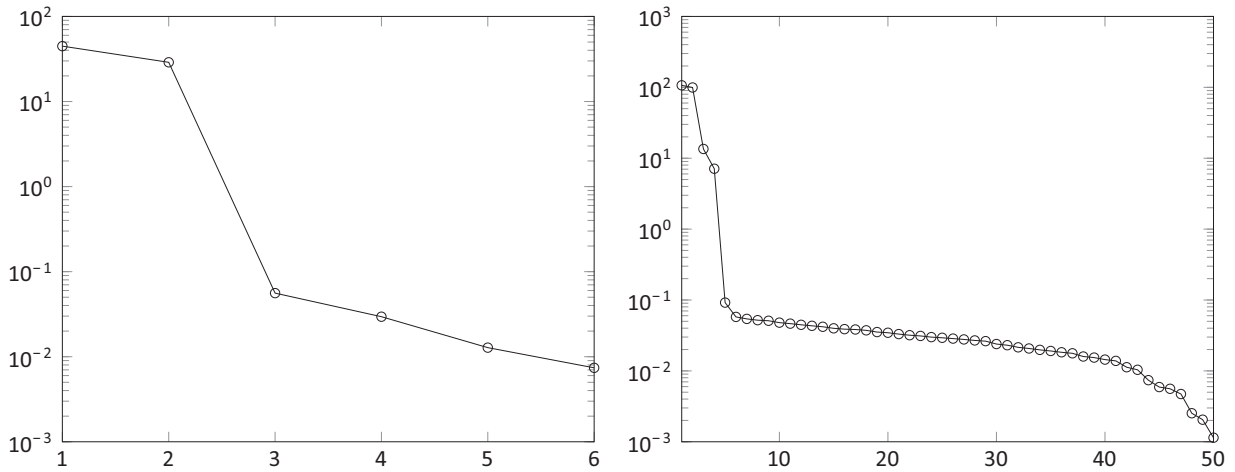
Fig. 2. Log-plot of singular values of $H_6^{(0)}$ and $H_{50}^{(0)}$ for $\phi(t)$ with added noise as described.

Another example illustrates the numerical behaviour of (4)–(5) in the case of clustered frequencies:

$$
\begin{aligned}
\phi_1 &= 0, & \alpha_1 &= 1, \\
\phi_2 &= -0.2 + \mathrm{i}39.5\pi, & \alpha_2 &= 2, \\
\phi_3 &= -0.5 + \mathrm{i}40\pi, & \alpha_3 &= 4, \\
\phi_4 &= -1 & \alpha_4 &= 8.
\end{aligned}
$$

We take the sampling interval $\Delta = 0.02$, which is in accordance with the Shannon–Nyquist requirement since $0.02 < 2\pi/\Omega = 0.025\pi$.

We then add some white circular Gaussian noise (mean 0, variance 1) which we normalize to have infinity-norm equal to 10^{-2}. Note that the frequencies appear in two clusters, one consisting of ϕ_1 and ϕ_4 with distinct damping but identical frequency, and one consisting of ϕ_2 and ϕ_3 with nearby frequencies. In Fig. 2 (left) we display the singular values of $H_\nu^{(0)}$ for $\nu = 6 > n = 4$. The log-scale plot indicates a numerical rank of 2 instead of the correct 4, revealing only the two clusters.

However, when we rewrite the exponential analysis problem in terms of Padé approximation using the reformulation presented below, the numerical rank will show up correctly. Besides finding the number of terms n, we also reconstruct [10,11] all the parameters in the representation (1) of $\phi(t)$ in some of the applications.

3. Exponential analysis viewed as Padé approximation

With $f_j = \phi(t_j)$ we now define the noisefree

$$
f(t) := \sum_{j=0}^{\infty} f_j t^j, \quad f^{(j)}(0) = f_j. \tag{8}
$$

The Padé approximant $r_{m,n}(t)$ of degree m in the numerator and n in the denominator to $f(t)$ is defined as the irreducible form of the rational function $p(t)/q(t)$ satisfying

$$
\frac{d^j (fq - p)(t)}{dt^j}(0) = 0, \quad j = 0, \ldots, m+n.
$$

With

$$
p(t) := \sum_{j=0}^{m} \pi_j t^j, \tag{9}
$$

$$
q(t) := \sum_{j=0}^{n} \rho_j t^j, \tag{10}
$$

this translates to

$$
\sum_{k=0}^{j} f_k \rho_{j-k} - \pi_j = 0, \quad j = 0, \ldots, m+n,
$$

where $\rho_j = 0$ for $j < 0$ and $\pi_j = 0$ for $j > m$. The condition essentially guarantees a high degree of contact between $f(t)$ and $p(t)/q(t)$. Since

$$f_j = \sum_{i=1}^{n} \alpha_i \exp(\phi_i j \Delta) = \sum_{i=1}^{n} \alpha_i \lambda_i^j,$$

we can rewrite

$$f(t) = \sum_{i=1}^{n} \frac{\alpha_i}{1 - t\lambda_i}. \tag{11}$$

So we see that, because of (2), $f(t)$ is itself a rational function of degree $n - 1$ in the numerator and n in the denominator, with poles $1/\lambda_i$. From Padé approximation theory we hence know that $r_{n-1,n}(t)$ computed for (8) reconstructs $f(t)$, in other words

$$r_{n-1,n}(t) = f(t).$$

The partial fraction decomposition (11) is related to the Laplace transform of the exponential model (1), which explains why this approach is known as the Padé–Laplace method.

3.1. Convergence of Padé approximants

Now we add a white circular Gaussian noise term ϵ_j to each sample f_j. In the sequel we denote the noisy series by

$$f(t) + \epsilon(t) = \sum_{j=0}^{\infty} (f_j + \epsilon_j) t^j.$$

A number of very nice approximation and convergence results exist for sequences of Padé approximants to $f(t) + \epsilon(t)$. They express what one would expect intuitively from such approximants: they are especially useful if the approximated function is meromorphic (i.e. has poles) in some substantial region of the complex plane, as is the case here.

Padé approximants are usually arranged in a table with the numerator degree m indicating the row number and the denominator degree n indicating the column number (or vice versa depending on the author). An important sequence of Padé approximants is the so-called diagonal sequence $\{r_{\nu,\nu}(t)\}_{\nu \in \mathbb{N}}$ in the table. Here we are interested in the adjacent para-diagonal sequence $\{r_{\nu-1,\nu}(t)\}_{\nu \in \mathbb{N}}$.

The theorem of Nuttall, later generalized by Pommerenke, states that if $f(t) + \epsilon(t)$ is analytic throughout the complex plane except for a countable number of poles [24] and essential singularities [28], then the paradiagonal sequence $\{r_{\nu-1,\nu}(t)\}_{\nu \in \mathbb{N}}$ converges to $f(t) + \epsilon(t)$ in measure on compact sets. So no assertion is made about pointwise or uniform convergence. Instead, the result states that for sufficiently large ν, the measure of the set where the convergence is disrupted, so where $|f(t) + \epsilon(t) - r_{\nu-1,\nu}(t)| \geq \tau$ for some given threshold τ, tends to zero as ν tends to infinity. The pointwise convergence is disrupted by $\nu - n$ unwanted pole-zero combinations of the Padé approximants $r_{\nu-1,\nu}(t)$: near each spurious pole introduced by increasing the denominator degree beyond the true n, one finds an associated zero, the pole and zero effectively cancelling each other locally. These pole-zero doublets are referred to as Froissart doublets [13,15,16].

Because of the Padé convergence theorem, the n true (physical) poles can be identified as stable poles in successive $r_{\nu-1,\nu}(t)$, while the $\nu - n$ spurious (noisy) poles are distinguished by their instability [3,26]. While the stable poles model the $\lambda_i, i = 1, \dots, n$ in the signal (1), the unstable poles model the additive noise. The physical poles reflect the structure present in the samples (2), the noisy poles the lack of it. So these Froissart doublets offer a way to separate or filter the noise $\epsilon(t)$ from the underlying $f(t)$ [5]. Note that we do not want to filter the samples $f_j + \epsilon_j$ before applying an exponential analysis method because this operation may at the same time destroy some of the structure in the data f_j.

Although in [17] and [20] the authors avoid the computation of Froissart doublets in a Padé approximation algorithm, another option is to make good use of their ability to model noise and only remove them at a later stage in the analysis, an approach we follow in this paper.

3.2. Illustration of the principle

To illustrate how to apply this idea we use our toy examples again. When computing the singular value decomposition of $H_\nu^{(0)}$ in the first example, containing a weak component, for $\nu = 100 \gg n = 4$, we see in Fig. 1 (right) that a numerical rank of 4 is now correctly indicated. Subsequently (6) and (7) of size ν can be solved to accurately obtain the parameters characterizing the n true components in (1). At this point it is again useful to compare our result to that of the algorithms in [17] and [20]: choosing the threshold parameter in [17] larger than or equal to 5×10^{-5} still returns a numerical rank for $H_{100}^{(0)}$ of 3, while putting it less than or equal to 1×10^{-6} returns the maximum value of 100 (for threshold values between 10^{-5} and 10^{-6} at least a numerical rank of 7 was returned).

When applying our approach to the second example, containing clustered frequencies, and computing the singular value decomposition of $H_\nu^{(0)}$ for $\nu = 50 \gg n = 4$, we see in Fig. 2 (right) that the correct numerical rank of 4 is again clearly revealed. And this rank does not change when ν is further increased.
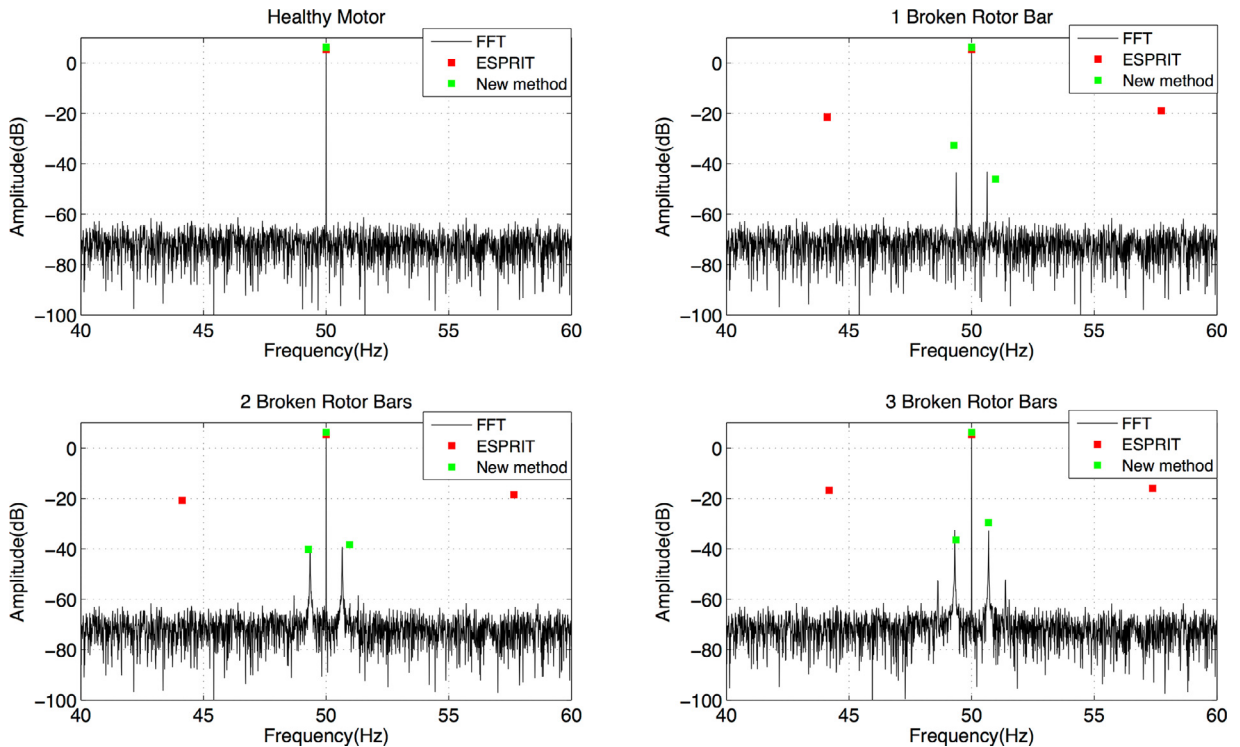
Fig. 3. MCSA at low load (10%) and high noise (16 dB). (For interpretation of the references to color in this figure, the reader is referred to the web version of this article.)

A practical application of our approach is presented in Section 4, where we are looking for faint components, and in Section 6, to correctly obtain the number of clustered components. The technique can also be applied when a component is strongly dominated by some other components, as in Section 5. Then again one needs to wait for the Padé approximation process to converge before the exact number of terms becomes clear and they can be identified. The parameters ϕ_i that we are looking for in the Sections 4, 5 and 6 are respectively purely imaginary numbers, purely real numbers and complex numbers.

The convergence can significantly be accelerated by combining it with an aliasing free uniform subsampling technique [10–12], if necessary in combination with some divide and conquer approach to keep the size of the Hankel matrices under control [7].

4. Scenario I: MCSA (imaginary ϕ_i)

We now present a situation in which the above is of particular interest. In diagnostics, the appearance of one or more additional, often undesirable, faint components in a spectrum may indicate that a fault is present or developing. We refer for instance to motor current signature analysis (MCSA) which inspects the frequency spectrum of a 3-phase induction motor's stator current signal to detect broken rotor bars. The frequency components of the stator current due to broken rotor bars in the induction motor are very close to the electrical supply frequency f_e (50/60 Hz) but much more faint. They are given by $(1 \pm 2ks)f_e$ where the harmonic frequency index $k = 1, 2, \ldots$ and the slip s [9] is given by

$$s = \frac{n_s - n_m(b)}{n_s}100\%.$$

Here n_s is the speed of the rotating magnetic field and $n_m(b)$ is the mechanical shaft speed of the motor that varies slightly with the number b of broken rotor bars. Broken rotor bars are difficult to diagnose under low load and high noise [33]. At the same time, detection of the faint sideband frequency components at low slip is identified as a major issue and should be addressed urgently [33]. Under low load, a high resolution Fourier analysis may not even reveal any additional frequencies besides the fundamental frequency, despite the presence of several broken rotor bars. Under full load, the fault is revealed easily. Alternatives such as wavelet based techniques are also reported to be unsatisfactory in the low slip case [22].

In Fig. 3 we present a typical stator current signal (the experiment was repeated a significant number of times) from a Simulink simulation (load 10%, noise 16 dB) [1]. The parameters used for the simulation are given in Table 1. The lower and higher sideband frequencies $f_e(1 - s)$ and $f_e(1 + s)$ are computed using a state-of-the-art implementation of the ESPRIT

Table 1
Induction motor simulation parameters.

Rated power	2200 W
Rated phase voltage	380 V
Rated frequency	50 Hz
Number of pole pairs	2
Stator winding resistance	2.33 Ohm
Stator winding inductance	13.78×10^{-3} H
Rotor winding resistance	2.18 Ohm
Rotor winding inductance	14.55×10^{-3} H
Mutual inductance	260.57×10^{-3} H
Moment of inertia	$0.089 \mathrm{kg} \cdot \mathrm{m}^2$
Fraction factor	0.005 Nms
Number of rotor bars	28

method (dark red) and compared to our new technique (light green). For ESPRIT (signal space dimension 40) as well as for the proposed approach ($\nu = 400 \gg 2k + 1$) 800 samples are collected at 256 Hz. The results are displayed together with a very high resolution Fourier analysis (100 s sampled at 2560 Hz) in order to obtain the ground truth. We merely show the frequency f_e of the electrical supply and the non-Froissart frequencies nearest to it, the first lower and higher sideband.

The new method on average picks up the two faint sidebands correctly, under low load and irrespective of the number of broken rotor bars, while the ESPRIT method is unable to pick up any of the faint components.

5. Scenario II: FLIM and MRI (real ϕ_i)

The next illustration concerns the relaxation model

$$B + A_1 \exp(-t/\tau_1) + A_2 \exp(-t/\tau_2) \tag{12}$$

which is often called a bi-exponential model (although $n = 3$ due to the constant term B). The term relaxation describes how signals change with time, meaning in general, how signals deteriorate with time. The model occurs in fluorescence lifetime imaging (FLIM) with $B = 0$, in magnetic resonance imaging (MRI) with $B \neq 0$ and several other applications. The time scale of the former may be as small as nanoseconds while that of the latter is milliseconds.

Fluorescence microscopy senses the fluorescence intensity of fluorescent molecules and can measure its decay rate or lifetime. Since this decay rate is sensitive to the cellular microenvironment, FLIM can be used to detect certain physiological or electrochemical parameters such as pH, oxygen level or temperature. The excited states of the fluorophores have lifetimes ranging from a few picoseconds to some tens of nanoseconds, which corresponds to the time scale of many important cellular interactions.

In MRI the term relaxation describes how signals decrease over time, more particularly, during the process in which spins dephase after a radiofrequency pulse because of spin-spin relaxation. MRI image contrast is influenced by several characteristics of tissues and other materials and this spin-spin relaxation. Often only a mono-exponential decay is assumed, although in tissue characterisation (myelin in the brain, breast tissue, cartilage, skeletal muscle, ...), typically two to four significant terms are present, indicating the multi-compartmental characteristics of the tissue.

The estimation of the relaxation parameters τ_1 and τ_2 and the corresponding amplitudes A_1 and A_2 is known to be difficult [6]. Moreover, when $0 < \tau_1 \ll \tau_2$, the term $A_2 \exp(-t/\tau_2)$ may be strongly dominated by the term $A_1 \exp(-t/\tau_1)$, almost until both disappear into the noise, as in Fig. 4.

We show that the presented technique is able to dig it up, when looking at approximants $r_{\nu-1,\nu}(t)$ of sufficiently high degree ν. In other words, when taking the dimension $\nu - n$ of the noise space large enough, so that the n physical poles in the z-transform of the exponential model have converged to sufficiently accurate values. To this end we perform the following experiments.

Consider (12) with $B = 0, A_1 = 174.13, A_2 = 19.348, \tau_1 = 22, \tau_2 = 80$. First, collect 256 samples at $t = j, j = 0, \ldots, 255$ and add 34 dB white Gaussian noise (in an MRI setting). The exponential terms and the noise are shown separately in Fig. 4. Second, with the same parameters and sampling, simulate photon count and apply Poisson noise of approximately 34 dB (in the FLIM setting). In Fig. 5 we show the log-plots of the singular values of $H_8^{(0)}$ (left) and $H_{36}^{(0)}$ (right) for the MRI setting. Similarly in Fig. 6, we show $H_8^{(0)}$ and $H_{42}^{(0)}$ for the FLIM setting. While in $H_8^{(0)}$, where ν is only slightly larger than $n = 2$, only one singular value clearly distantiates itself from the noise, in $H_{36}^{(0)}$ and $H_{42}^{(0)}$ on the other hand, where ν is significantly larger than $n = 2$, it becomes two singular values.

In the above relaxometry experiment, the new technique is able to detect and identify the faint component in which one is interested, while in a classical approach one is unaware of its existence.

6. Scenario III: MRS (complex ϕ_i)

The data measured from magnetic resonance spectroscopy (MRS) are damped time signals, called free induction decay (FID). MRS is a powerful tool for the non-invasive analysis of the biochemical composition of tissues in vivo and to
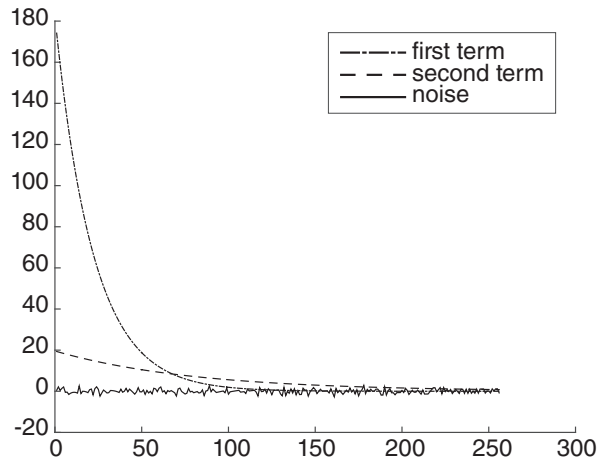
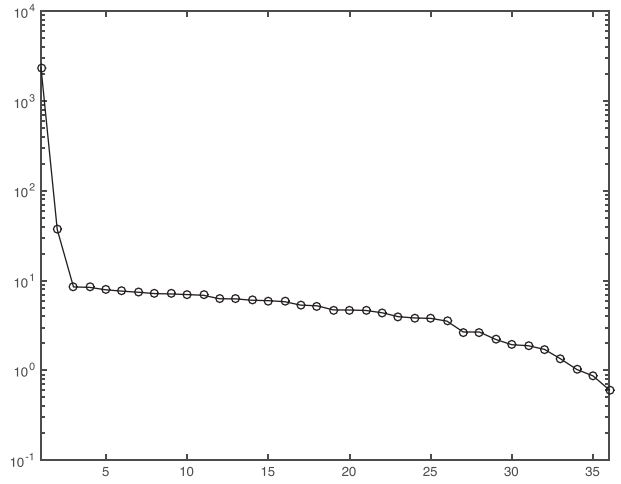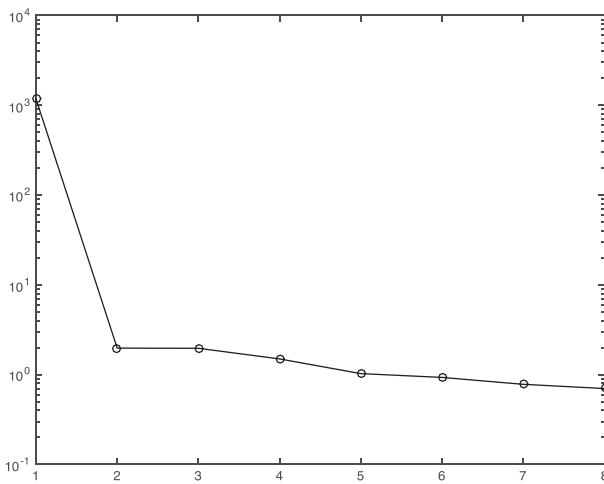**Fig. 4.** Individual components in (12) including the discrete noise.

Fig. 5. Log-plot of singular values of $H_8^{(0)}$ and $H_{36}^{(0)}$ with 34 dB white Gaussian noise added to (12).
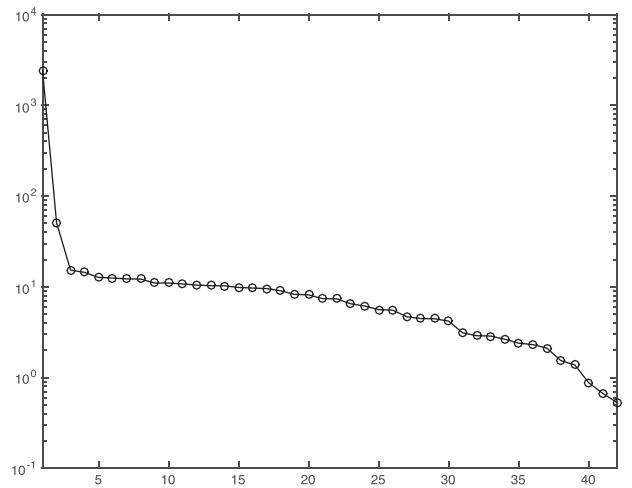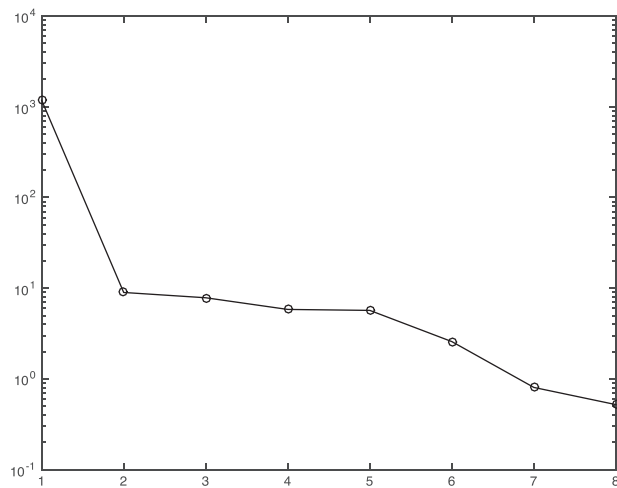

Fig. 6. Log-plot of singular values of $H_8^{(0)}$ and $H_{42}^{(0)}$ for photon count simulation following (12) with approximately 34 dB noise.

Table 2
Example signal contains 25 components occurring in 6 clusters.

Cluster	damping/frequency	amplitude/phase
I	$\phi_1 = -0.07 - \mathrm{i}707.8\pi$	$\alpha_1 = 0.77\exp(\mathrm{i}0.15)$
	$\phi_2 = -0.132 - \mathrm{i}704.04\pi$	$\alpha_2 = 6.2$
	$\phi_3 = -0.1 - \mathrm{i}698.84\pi$	$\alpha_3 = 0.98\exp(\mathrm{i}0.3)$
	$\phi_4 = -0.11 - \mathrm{i}696.02\pi$	$\alpha_4 = 5.4\exp(\mathrm{i}0.9)$
	$\phi_5 = -0.12 - \mathrm{i}694.02\pi$	$\alpha_5 = 6.1\exp(\mathrm{i}0.7)$
	$\phi_6 = -0.081 - \mathrm{i}690\pi$	$\alpha_6 = 0.95\exp(\mathrm{i}0.2)$
II	$\phi_7 = -0.106 - \mathrm{i}265\pi$	$\alpha_7 = 4.71\exp(\mathrm{i}0.12)$
	$\phi_8 = -0.129 - \mathrm{i}262.8\pi$	$\alpha_8 = 3.9\exp(\mathrm{i}0.1)$
	$\phi_9 = -0.203 - \mathrm{i}260.02\pi$	$\alpha_9 = 7.0\exp(-\mathrm{i}0.234)$
	$\phi_{10} = -0.16 - \mathrm{i}258.34\pi$	$\alpha_{10} = 5.43\exp(\mathrm{i}0.2)$
	$\phi_{11} = -0.19 - \mathrm{i}256.18\pi$	$\alpha_{11} = 4.4\exp(-\mathrm{i}0.52)$
III	$\phi_{12} = -0.102 + \mathrm{i}28.2\pi$	$\alpha_{12} = 3\exp(\mathrm{i}0.21)$
	$\phi_{13} = -0.127 + \mathrm{i}31.62\pi$	$\alpha_{13} = 3\exp(-\mathrm{i}0.8)$
IV	$\phi_{14} = -0.076 + \mathrm{i}215.4\pi$	$\alpha_{14} = 0.39\exp(-\mathrm{i}0.3)$
	$\phi_{15} = -0.091 + \mathrm{i}220.48\pi$	$\alpha_{15} = 0.37\exp(-\mathrm{i}0.8)$
	$\phi_{16} = -0.1 + \mathrm{i}225\pi$	$\alpha_{16} = 0.36\exp(\mathrm{i}0.1)$
	$\phi_{17} = -0.08 + \mathrm{i}228\pi$	$\alpha_{17} = 0.3\exp(\mathrm{i}0.9)$
V	$\phi_{18} = -0.21 + \mathrm{i}248.02\pi$	$\alpha_{18} = 3.2\exp(-\mathrm{i}0.106)$
	$\phi_{19} = -0.15 + \mathrm{i}251.24\pi$	$\alpha_{19} = 5.53\exp(\mathrm{i}0.2)$
	$\phi_{20} = -0.173 + \mathrm{i}253.96\pi$	$\alpha_{20} = 4.7\exp(-\mathrm{i}0.3)$
VI	$\phi_{21} = -0.11 + \mathrm{i}868\pi$	$\alpha_{21} = \exp(-\mathrm{i}0.15)$
	$\phi_{22} = -0.12 + \mathrm{i}870.76\pi$	$\alpha_{22} = 5\exp(\mathrm{i}0.26)$
	$\phi_{23} = -0.157 + \mathrm{i}872.38\pi$	$\alpha_{23} = 6.1\exp(-\mathrm{i}0.2)$
	$\phi_{24} = -0.12 + \mathrm{i}875.94\pi$	$\alpha_{24} = 5.1$
	$\phi_{25} = -0.18 + \mathrm{i}879.02\pi$	$\alpha_{25} = 6\exp(-\mathrm{i}0.1)$
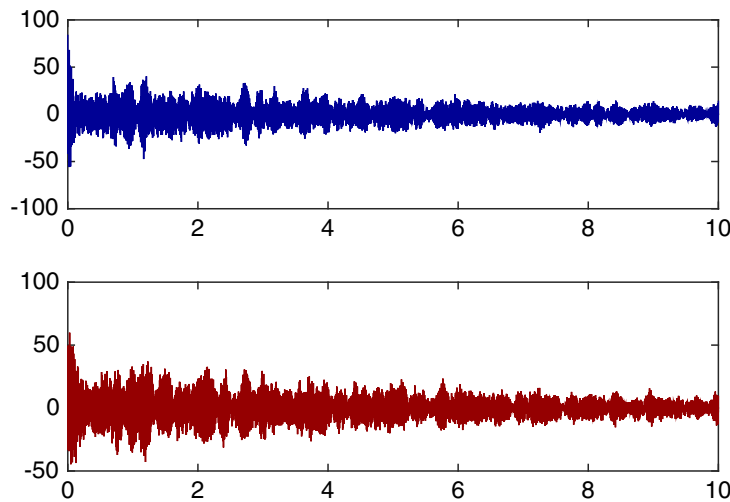
Fig. 7. Real and imaginary part of synthesized FID signal.

characterize functional metabolic processes in different parts of the body (brain, muscles, organs, ...). Using Fourier based methods, the detection of some metabolites in the spectrum is however hampered by spectral overlap with other metabolites (such as, for instance, glutamate and glutamine). This limitation makes the data hard to interpret. So researchers have to turn their attention to other methods, as it may be crucial to separate metabolites in the spectrum (it was found, for instance, that reduced glutamate in the human motor cortex is, among other things, consistent with neuronal loss or shrinkage with age). So the importance of these analyses cannot be overstated.

When turning to the parametric method of exponential analysis, usually prior knowledge of the model order is required [30]. Our method precisely provides the latter. We illustrate, on synthesized MRS data, the correct model order detection in the case of a signal containing several closeby frequencies. For the details about the frequencies, damping factors, phases and amplitudes in the different clusters, we refer to Table 2. Our example signal contains 25 components occurring in 6 clusters with, in addition, several of them containing weak elements (so the correct model order is really hard to get):

- There are 3 weak components in the first cluster.
- The fourth cluster consists entirely of weak components.
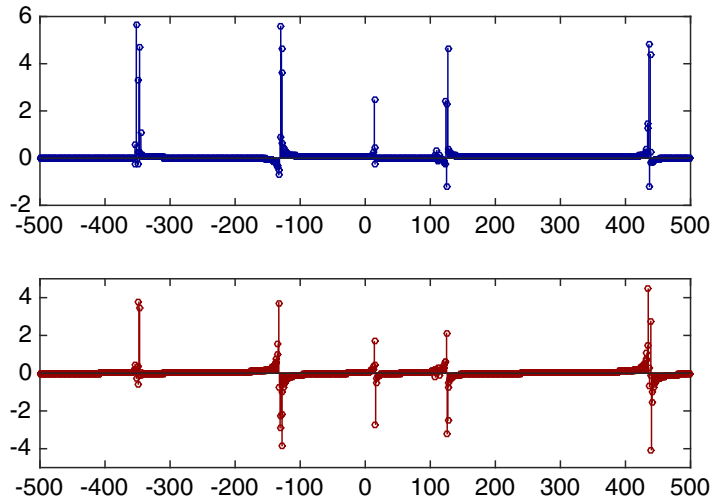- There is 1 weaker component in the sixth cluster.

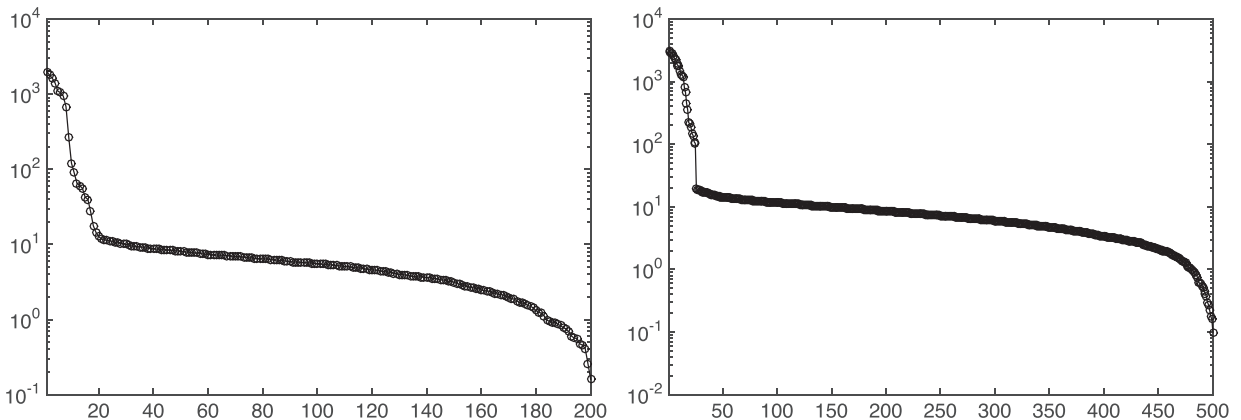**Fig. 8.** Real and imaginary part of FFT of synthesized FID signal.

Fig. 9. Log-plot of singular values of $H_{200}^{(0)}$ and $H_{500}^{(0)}$ with normalized noise added to synthesized FID.

We take the sampling interval $\Delta = 0.001$, which is in accordance with the Shannon–Nyquist requirement since $0.001 < 2\pi/\Omega = 0.001138$. To each signal sample white circular Gaussian noise (mean 0, variance 1) is added, normalized to have infinity-norm equal to $\epsilon = 1 \times 10^0$ (35 dB). Fig. 7 shows the real and imaginary part of the resulting synthesized signal. A Fourier analysis based on 1000 samples, shown in Fig. 8, reveals only 5 clusters as the cluster of weak elements is entirely overtaken by the noise. Besides that, the exact number of components is not at all clear from the analysis. Also, in the singular value decomposition of $H_{200}^{(0)}$ (Fig. 9, left) the correct model order is not visible. However, from the singular value decomposition of $H_{500}^{(0)}$ (Fig. 9, right) requiring 999 signal samples, it is obvious.

7. Conclusion

In these experiments we combine the Padé view on exponential analysis with some well-known convergence theorems for Padé approximants in order to achieve a better separation of signal and noise. We let the Froissart doublets, which appear in addition to the true physical poles of the rational function $f(t)$ as a consequence of the noise $\epsilon(t)$, model the noise, rather than that we avoid their computation. This leads to more accuracy in higher degree approximants. Faint components that are discarded in lower degree approximations where the computation of the Froissart doublets is avoided, can now be picked up very reliably.

We illustrated the usefulness of the technique in three applications: motor current signature analysis (MCSA), magnetic resonance imaging (MRI) or fluorescence lifetime imaging (FLIM), and magnetic resonance spectroscopy (MRS).

Acknowledgments

References

[1] M. Akar, Detection of rotor bar faults in field oriented controlled induction motors, J. Power Electron. 12 (6) (2012) 982–991.
[2] Z. Bajzer, A.C. Myers, S.S. Sedarous, F.G. Prendergast, Padé–Laplace method for analysis of fluorescence intensity decay, Biophys. J. 56 (1) (1989) 79–93.
[3] P. Barone, On the distribution of poles of Padé approximants to the Z-transform of complex Gaussian white noise, J. Approx. Theory 132 (2) (2005) 224–240.
[4] M. Bertero, P. Boccacci, E.R. Pike, F.R.S., on the recovery and resolution of exponential relaxation rates from experimental data: a singular-value analysis of the Laplace transform inversion in the presence of noise, Proc. R. Soc. Lond. A 383 (1784) (1982) 15–29.
[5] D. Bessis, Padé approximations in noise filtering, J. Comput. Appl. Math. 66 (1–2) (1996) 85–88.
[6] M. Björk, D. Zachariah, J. Kullberg, P. Stoica, A multicomponent T_2 relaxometry algorithm for myelin water imaging of the brain, Magn. Reson. Med. 75 (1) (2016) 390–402.
[7] M. Briani, A. Cuyt, W.-s. Lee, V.P. Gerdt, W. Koepf, W.M. Seiler, W.M. Vorozhtsov, Sparse interpolation, the FFT algorithm and FIR filters, in: Proceedings of the Computer Algebra in Scientific Computing, Springer, Cham, Switzerland, 2017, pp. 27–39.
[8] E.J. Candès, C. Fernandez-Granda, Towards a mathematical theory of super-resolution, Commun. Pure Appl. Math. 67 (6) (2014) 906–956.
[9] S.J. Chapman, Electric Machinery Fundamentals, fourth ed., Tata McGraw-Hill Education, 2005.
[10] A. Cuyt, W.-S. Lee, Smart data sampling and data reconstruction, US Patent 9,690,749, 2017. June 27, 2017.
[11] A. Cuyt, W.-S. Lee, Smart data sampling and data reconstruction, Patent PCT/EP2012/066204, EP 20,120,762,227. December 21, 2016.
[12] A. Cuyt, W.-S. Lee, How to get high resolution results from sparse and coarsely sampled data, 2017, ArXiv: 1710.09694 [math.NA].
[13] J. Gammel, P.R. Graves-Morris, Effect of Random Errors (noise) in the Terms of a Power Series on the Convergence of the Padé Approximants, The Institute of Physics, London, England, 1973, 132–133. Padé approximants.
[14] M. Giesbrecht, G. Labahn, W.-S. Lee, Symbolic-numeric sparse interpolation of multivariate polynomials, J. Symb. Comput. 44 (8) (2009) 943–959.
[15] J. Gilewicz, M. Pindor, Padé approximants and noise: a case of geometric series, J. Comput. Appl. Math. 87 (2) (1997) 199–214.
[16] J. Gilewicz, M. Pindor, Padé approximants and noise: rational functions, J. Comput. Appl. Math. 105 (1–2) (1999) 285–297.
[17] P. Gonnet, S. Güttel, L.N. Trefethen, Robust Padé approximation via SVD, SIAM Rev. 55 (1) (2013) 101–117.
[18] P. Henrici, Applied and computational complex analysis, in: Volume 1: Power Series-Integration-Conformal Mapping-Location of Zeros, John Wiley & Sons, New York, 1974.
[19] Y. Hua, T.K. Sarkar, Matrix pencil method for estimating parameters of exponentially damped/undamped sinusoids in noise, IEEE Trans. Acoust. Speech Signal Process. 38 (5) (1990) 814–824.
[20] O.L. Ibryaeva, V.M. Adukov, An algorithm for computing a Padé approximant with minimal degree denominator, J. Comput. Appl. Math. 237 (1) (2013) 529–541.
[21] E. Kaltofen, W.-S. Lee, A.A. Lobo, Early termination in Ben-Or/Tiwari sparse interpolation and a hybrid of Zippel's algorithm, in: C. Traverso (Ed.), Proceedings of the International Symposium on Symbolic and Algebraic Computation (ISSAC 2000), ACM, New York, NY, USA, 2000, pp. 192–201.
[22] Y.-H. Kim, Y.-W. Youn, D.-H. Hwang, J.-H. Sun, D.-S. Kang, High-resolution parameter estimation method to identify broken rotor bar faults in induction motors, IEEE Trans. Ind. Electron. 60 (9) (2013) 4103–4117.
[23] S.Y. Kung, K.S. Arun, D.V.B. Rao, State-space and singular-value decomposition-based approximation methods for the harmonic retrieval problem, J. Opt. Soc. Am. 73 (12) (1983) 1799–1811.
[24] J. Nuttall, The convergence of Padé approximants of meromorphic functions, J. Math. Anal. Appl. 31 (1) (1970) 147–153.
[25] H. Nyquist, Certain topics in telegraph transmission theory, Trans. Am. Ins. Electr. Eng. 47 (2) (1928) 617–644.
[26] L. Perotti, T. Regimbau, D. Vrinceanu, D. Bessis, Identification of gravitational-wave bursts in high noise using Padé filtering, Phys. Rev. D 90 (2014) 124047.
[27] V.F. Pisarenko, The retrieval of harmonics from a covariance function, Geophys. J. R. Astron. Soc. 33 (3) (1973) 347–366.
[28] C. Pommerenke, Padé approximants and convergence in capacity, J. Math. Anal. Appl. 41 (3) (1973) 775–780.
[29] R. de Prony, Essai expérimental et analytique sur les lois de la dilatabilité des fluides élastiques et sur celles de la force expansive de la vapeur de l'eau et de la vapeur de l'alkool, à différentes températures, J. de l'École Polytechnique 1 (1795) 24–76.
[30] R. Roy, T. Kailath, ESPRIT-estimation of signal parameters via rotational invariance techniques, IEEE Trans. Acousti. Speech Signal Process. 37 (7) (1989) 984–995.
[31] R. Schmidt, Multiple emitter location and signal parameter estimation, IEEE Trans. Antennas Propag. 34 (3) (1986) 276–280.
[32] C.E. Shannon, Communication in the presence of noise, Proc. IRE 37 (1) (1949) 10–21.
[33] B. Xu, L. Sun, L. Xu, G. Xu, Improvement of the Hilbert method via ESPRIT for detecting rotor fault in induction motors at low slip, IEEE Trans. Energy Convers. 28 (1) (2013) 225–233.
[34] Y. Zhang, A. Cuyt, W.-s. Lee, G. Lo Bianco, G. Wu, Y. Chen, D.D. Li, Towards unsupervised fluorescence lifetime imaging using low-dimensional variable projection, Opt. Express 24 (23) (2016) 26777–26791.